Highly efficient quantum Stirling engine using multilayer Graphene

Bastian Castorene,[1,2,*] Francisco J. Peña,[2] Eric Suarez,[2] Caio Lewenkopf,[3]
Martin HvE Groves,[2] Natalia Cortés,[2] and Patricio Vargas[2]

[1] *Instituto de Física, Pontificia Universidad Católica de Valparaíso, Casilla 4950, 2373223 Valparaíso, Chile*
[2] *Departamento de Física, Universidad Técnica Federico Santa María, 2390123 Valparaíso, Chile*
[3] *Instituto de Física, Universidade Federal do Rio de Janeiro, Rio de Janeiro, RJ 21941-972, Brazil*

(Dated: October 22, 2025)

In this work, quantum Stirling engines based on monolayer, AB-stacked bilayer, and ABC-stacked trilayer graphene under perpendicular magnetic fields are analyzed. Performance maps of the useful work (ηW) reveal a robust optimum at low magnetic fields and moderately low temperatures, with all stackings capable of reaching Carnot efficiency under suitable configurations. The AB bilayer achieves this across the broadest parameter window while sustaining finite work, the monolayer exhibits highly constrained regimes, and the trilayer shows smoother trends with sizable ηW. These results identify multilayer graphene, particularly the AB bilayer, as a promising platform for efficient Stirling engines, while also highlighting the versatility of the monolayer in realizing all four operational regimes of the Stirling cycle.

PACS numbers:

I. INTRODUCTION

Quantum thermodynamics examines how the fundamental principles of energy transfer, heat exchange, and entropy apply to small systems where quantum effects such as coherence, entanglement, spin correlations, and discrete energy levels give rise to thermodynamical properties with no classical counterpart, and where quantum statistics provides a natural framework to describe these phenomena [1–15].

In this context, considerable attention has been devoted to understanding how quantum systems, such as trapped ions, superconducting qubits, quantum dots, and low-dimensional electronic materials and their diverse behaviors can be harnessed to implement heat engines capable of producing useful work. Among quantum thermal machines, the Stirling cycle has attracted particular interest due to its potential to achieve high efficiency in regimes where thermalization and isochoric processes can be controlled with precision [16–32]. In light of these considerations, theoretical and experimental investigations have shown that quantum heat engines based on discrete energy spectra may surpass their classical counterparts in specific regimes, particularly when the working substance exhibits a tunable energy level structure and distinctive statistical properties [33, 34]. Within this framework, graphene and its multilayer stacks under perpendicular magnetic fields stand out as promising platforms due to their unique Landau level spectra [35–39], combined with their ease of fabrication and precise experimental control [40–51].

In this regard, several studies have proposed graphene-based systems, including quantum dots and multilayer structures, as candidates for quantum engines [52–62]. It is important to emphasize that many previous studies rely exclusively on Boltzmann statistics and employ simplified descriptions that neglect the fermionic nature of the electronic working fluid in graphene [7, 41, 42, 63]. In contrast, the present analysis explicitly incorporates the Fermi–Dirac statistics of charge carriers under realistic doping and experimental conditions. Moreover, the large degeneracy of the Landau levels implies that the number of participating electrons can be very high, providing a unique framework to explore quantum corrections to thermodynamic quantities arising from the discreteness of the Landau-level spectrum while remaining within the thermodynamic limit. As a result, thermal fluctuations are strongly suppressed, making it possible to isolate genuine quantum effects from those associated with finite-size fluctuations.

This study examines the quantum Stirling cycle using monolayer, AB-stacked bilayer, and ABC-stacked trilayer graphene under perpendicular magnetic fields as the working medium. By incorporating Fermi–Dirac statistics into the thermodynamic description, the analysis provides a realistic account of electronic population dynamics, particularly at low temperatures and finite doping, extending beyond the idealized charge-neutrality point and enhancing the relevance of the results to experimental conditions. Within a grand-canonical formalism, thermodynamic quantities such as internal energy and entropy are evaluated, accounting for the symmetries specific to each multilayer configuration.

The chemical potential μ is determined self-consistently throughout the cycle to ensure particle-number conservation, enabling a consistent realization of the Stirling cycle with the magnetic field as the external control parameter and the system evolving through isothermal and isomagnetic strokes. The analysis reveals that the distinct Landau levels spectra of monolayer, bilayer, and trilayer graphene systems determine the heat exchanged during the cycle and, consequently, the result-

*Electronic address: bastian.castorene.c@mail.pucv.cl

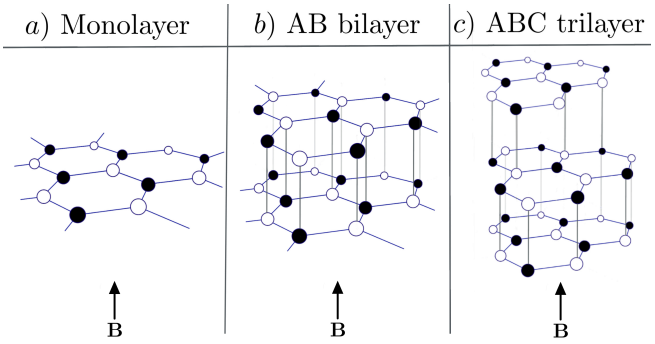

FIG. 1: Schematic representation of the lattice structure of graphene multilayer systems (under a perpendicular homogeneous magnetic field B). Panel (a) shows the monolayer, panel (b) the AB-stacked bilayer, and panel (c) the ABC-stacked trilayer.

ing efficiency and performance. Among these systems, AB-stacked bilayer graphene provides the most favorable regime, combining high efficiency with finite work output.

The structure of the paper is as follows. Section II introduces the theoretical framework and the Landau level spectra for graphene with different multilayer stackings. Section III derives the thermodynamic functions required to implement the Stirling cycle. Section IV presents the analysis of efficiency and work output across different regimes. Finally, Sec. V presents the conclusions with a summary and possible extensions.

II. THEORY AND METHODS

A. Landau Level Spectrum in Multilayer Graphene

At low electronic doping, within the low-energy approximation where a Dirac-like equation provides an accurate description of the electronic properties of graphene, the Landau level spectra of multilayer structures in a perpendicular magnetic field can be expressed through simple analytical formulas [37–39]. These relations are written in terms of the Fermi velocity $v_F \simeq 3\times10^6$ [m/s], the elementary charge e, the Planck constant $\hbar$, the Landau level index n, and the external magnetic-field strength B.

1. *Landau Level Spectrum of Monolayer Graphene*

Monolayer graphene is a single layer of sp^2-hybridized carbon atoms arranged in a two-dimensional honeycomb lattice. The primitive unit cell of this structure contains two inequivalent sites, A and B, corresponding to the filled and empty circles in Fig. 1(a). The corresponding reciprocal lattice is also honeycomb, featuring two inequivalent points, K and K', in the Brillouin zone [35]. Each carbon atom contributes one electron to the valence and conduction bands. Remarkably, the low-energy electronic structure exhibits a linear dispersion relation, $\varepsilon_{\mathbf{k}} = \hbar v_F|\mathbf{k}|$, centered at the K and K' symmetry points. This behavior is characteristic of massless Dirac fermions [35].

When subjected to a perpendicular magnetic field B, these ultrarelativistic quasiparticles exhibit a unique Landau-level spectrum given by [35]

$$\varepsilon^{(1)}_{n,\pm} = \pm\hbar\omega^{(1)}_c\sqrt{n}, \quad n = 0,1,2,\ldots, \tag{1}$$

where the characteristic cyclotron frequency is

$$\omega^{(1)}_c = \sqrt{\frac{2ev_F^2B}{\hbar}}. \tag{2}$$

A distinctive feature of this spectrum is the presence of a zero-energy Landau level ($n = 0$) shared equally by electrons and holes. Unlike conventional two-dimensional electron gases, here the Landau levels are not equally spaced but instead scale proportional to $\sqrt{nB}$, a direct consequence of the massless Dirac-like Hamiltonian that effectively describes the electronic dynamics at low energies and at $B = 0$.

These features give rise to a fourfold-degenerate zero-energy state, originating from the spin and valley degrees of freedom, while higher Landau levels preserve the same degeneracy. This aspect will be further addressed in the following section, where it plays a central role in the formulation of the grand partition function. The resulting spectral asymmetry and nonuniform level spacing have profound implications for both the quantum Hall effect and the thermodynamic behavior of monolayer graphene [47, 48, 64, 65].

2. *Landau Level Spectrum of AB-Stacked Bilayer Graphene*

In AB-stacked bilayer graphene, shown in Fig. 1(b), the low-energy excitations correspond to massive chiral quasiparticles, whose pseudospin is locked to the momentum orientation due to the interlayer coupling. Under the application of a perpendicular magnetic field B, their corresponding Landau level spectrum is described by [37]

$$\varepsilon^{(2)}_{n,\pm} = \pm\hbar\omega^{(2)}_c\sqrt{n(n-1)}, \quad n = 0,1,2,\ldots, \tag{3}$$

where the effective cyclotron frequency $\omega^{(2)}_c$ and effective mass m^* are, respectively

$$\omega^{(2)}_c = \frac{eB}{m^*} \qquad \text{and} \qquad m^* = \frac{t_\perp}{2v_F^2}. \tag{4}$$

Here, the dominant interlayer hopping parameter is $t_\perp \simeq 0.39\,\text{eV}$, which yields an effective mass $m^* \simeq 0.0343\,m_e$. In contrast to monolayer systems, not only $n = 0$ forms a zero-energy Landau level, but also $n = 1$, leading to a twofold degeneracy of the zero mode that

is further enlarged by spin and valley symmetries. For $n \geq 2$, the Landau levels are unequally spaced and increase approximately linearly with B, in contrast to the $\sqrt{B}$-scaling observed in the monolayer. This spectral structure plays a central role in determining the thermodynamic and transport properties of bilayer graphene under perpendicular magnetic fields [37].

3. *Landau Level Spectrum of ABC-Stacked Trilayer Graphene*

In ABC-stacked (rhombohedral) trilayer graphene, shown in Fig. 1(c), the low-energy bands follow a cubic dispersion $E \propto k^3$, in contrast to the linear and quadratic cases discussed previously. Under a perpendicular magnetic field B, the Landau levels are given by [51]

$$\varepsilon_{n,\pm}^{(3)} = \pm\hbar\omega_c^{(3)}\sqrt{n(n-1)(n-2)}, \quad n \in \{0,1,2,\dots\}, \tag{5}$$

where the cyclotron frequency is

$$\omega_c^{(3)} = \frac{\left(2eBv_F^2\right)^{3/2}\sqrt{\hbar}}{t_\perp^2} \tag{6}$$

Here, v_F denotes the Fermi velocity and $t_\perp \simeq 0.3\,\mathrm{eV}$ is the dominant interlayer hopping parameter.

This spectrum exhibits the characteristic scaling $\varepsilon_n \propto B^{3/2}$, consistent with cubic-dispersion models reported in the literature. The first three levels ($n = 0, 1, 2$) collapse to zero energy, increasing the zero-mode degeneracy. For $n \geq 3$, the levels become non-equidistant and increasingly spaced, while remaining compressed compared to bilayer systems due to the $\sqrt{n(n-1)(n-2)}$ dependence.

Since the Landau-level spectra are analytically well established for all three systems, a sufficiently large yet finite number of levels is included in the calculations to ensure numerical convergence over the relevant temperature and magnetic-field ranges.

III. THERMODYNAMIC DESCRIPTION OF MULTILAYER GRAPHENE SYSTEMS UNDER MAGNETIC FIELD

A. Grand canonical formalism

The thermodynamic properties of electrons in graphene multilayer systems under perpendicular magnetic fields are naturally described within the grand-canonical ensemble, where both the temperature T and the chemical potential μ serve as control parameters. In this framework, the central quantities of interest are the internal energy U, the entropy S, and the particle number $\langle N\rangle$, which together determine the efficiency and work output of thermal cycles.

For multilayer graphene with quantized Landau levels $\varepsilon_{n,\pm}^{(i)}$ (with $i = 1, 2, 3$ denoting monolayer, bilayer, and trilayer), the grand-canonical partition function can be written explicitly as

$$\mathcal{Z}^{(i)} = \prod_{n,\pm}\left[1 + e^{-\beta\left(\varepsilon_{n,\pm}^{(i)} - \mu\right)}\right]^{g_n^{(i)}}, \tag{7}$$

For the Landau-level energies defined in Eqs. (1), (3), and (5), the corresponding degeneracies $g_n^{(i)}$ are given by

- For all levels with $n \geq 1$ have degeneracy $g_n^{(i)} = 4$.
- The zero-energy level ($n = 0$) exhibits enhanced degeneracy:

$$g_0^{(1)} = 4, \qquad g_0^{(2)} = 8, \qquad g_0^{(3)} = 12. \tag{8}$$

Taking these degeneracies into account, the grand potential can be expressed as

$$\Omega^{(i)} = -k_B T \sum_{n,\pm} g_n^{(i)} \ln\left[1 + e^{-\beta\left(\varepsilon_{n,\pm}^{(i)} - \mu\right)}\right], \tag{9}$$

from which the thermodynamic quantities follow as

$$\langle N\rangle = -\frac{\partial\Omega^{(i)}}{\partial\mu}\bigg|_T, \quad S = -\frac{\partial\Omega^{(i)}}{\partial T}\bigg|_\mu, \quad U = \Omega^{(i)} + TS + \mu\langle N\rangle. \tag{10}$$

Equivalently, one may start from the Fermi–Dirac distribution, which gives the occupation of each single-particle state,

$$f(\varepsilon,\mu,T) = \frac{1}{e^{\beta(\varepsilon-\mu)}+1}, \qquad \beta = \frac{1}{k_B T}, \tag{11}$$

together with the density of states (DOS),

$$\nu^{(i)}(\varepsilon) = \sum_{n,\pm} g_n^{(i)}\,\delta(\varepsilon - \varepsilon_{n,\pm}^{(i)}). \tag{12}$$

This allows the same observables to be written as

$$\langle N(\mu,T)\rangle = \int_{-\infty}^{\infty} d\varepsilon\,\nu^{(i)}(\varepsilon)\,f(\varepsilon,\mu,T), \tag{13}$$

$$U(\mu,T) = \int_{-\infty}^{\infty} d\varepsilon\,\nu^{(i)}(\varepsilon)\,\varepsilon\,f(\varepsilon,\mu,T), \tag{14}$$

$$S(\mu,T) = -k_B \int_{-\infty}^{\infty} d\varepsilon\,\nu^{(i)}(\varepsilon)\,\left[f\ln f + (1-f)\ln(1-f)\right]. \tag{15}$$

Both approaches are formally equivalent: the discrete-level formulation based on the grand potential and the continuum representation using the DOS combined with the Fermi–Dirac distribution, both yielding to identical thermodynamic quantities. It is worth emphasizing that the DOS representation makes explicit the role of Landau-level degeneracies, particularly the zero-energy states in all systems. For the purposes of this work, we adopt the latter approach in our calculations.

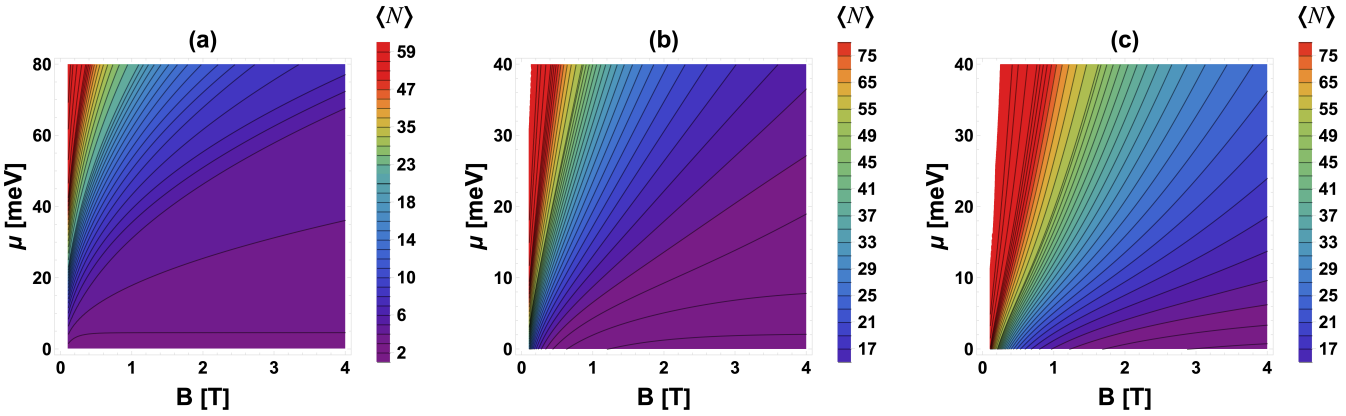

FIG. 2: Color map of the total number of electrons $\langle N\rangle$ as a function of magnetic field $B\,[T]$ and chemical potential μ [meV] for (a) monolayer, (b) bilayer and (c) trilayered graphene system under a fixed temperature $T = 50$ K.

B. Energy Scales and Parametrization of the Chemical Potential to Conserve Particle Number

Having established the theoretical framework, we now estimate the order of magnitude of the energy separation between the ground state and the first accessible Landau excitation as the magnetic field B is varied. This quantity (Δ) sets the relevant energy scale for the thermodynamic analysis, since it determines the temperatures required to thermally populate excited states as the field is varied [35, 37, 38, 51].

In monolayer graphene, the spacing between the ground and first excited Landau levels can be expressed as

$$\Delta_{\rm mono}(B) = \hbar\omega_c^{(1)} \simeq 36.3\sqrt{B}\left[\frac{\rm meV}{\sqrt{\rm T}}\right]. \qquad (16)$$

yielding $\Delta_{\rm mono}(1\,{\rm T}) \approx 36.3\,{\rm meV}$, $\Delta_{\rm mono}(3.11\,{\rm T}) \approx 64.0\,{\rm meV}$, and $\Delta_{\rm mono}(5\,{\rm T}) \approx 81.2\,{\rm meV}$.

In AB–stacked bilayer graphene, described at low energies by a parabolic band with effective mass m^*, the first nonzero Landau level appears at $n = 2$. The corresponding separation is

$$\Delta_{\rm bi}(B) = \hbar\omega_c^{(2)} \simeq 4.77 \times B\left[\frac{\rm meV}{\rm T}\right]. \qquad (17)$$

which gives $\Delta_{\rm bi}(1\,{\rm T}) \approx 4.77\,{\rm meV}$, $\Delta_{\rm bi}(3.11\,{\rm T}) \approx 14.8\,{\rm meV}$, and $\Delta_{\rm bi}(5\,{\rm T}) \approx 23.9\,{\rm meV}$.

For rhombohedral (ABC) trilayer graphene, the first accessible excitation occurs at $n = 3$, with

$$\Delta_{\rm tri}(B) = \hbar\omega_c^{(3)} \simeq 0.771 \times (B)^{3/2}\left[\frac{\rm meV]}{T^{3/2}}\right]. \qquad (18)$$

leading to $\Delta_{\rm tri}(1\,{\rm T}) \approx 0.77\,{\rm meV}$, $\Delta_{\rm tri}(3.11\,{\rm T}) \approx 4.23\,{\rm meV}$, and $\Delta_{\rm tri}(5\,{\rm T}) \approx 8.62\,{\rm meV}$.

Within the field range 0.1–5 T, the energy separation between consecutive Landau levels in the trilayer remains consistently smaller than in the bilayer and well below that of the monolayer. This hierarchy implies that monolayer graphene requires substantially higher temperatures to thermally populate its first excited Landau level, whereas the trilayer can achieve full population at comparatively lower temperatures.

Since the thermodynamic quantities explicitly depend on the energy levels through the chemical potential, it is essential to examine how μ evolves with the magnetic field B. To this end, we study the total particle number $\langle N\rangle$, whose dependence on B and μ provides indirect yet crucial information about the chemical potential. This behavior is shown in Fig. 2, which presents contour plots of $\langle N\rangle$ as a function of the magnetic field for monolayer (a), bilayer (b), and trilayer (c) graphene at a fixed temperature $T = 50\,{\rm K}$.

In Fig. 2(a), the monolayer exhibits contours of $\langle N\rangle$ that approximately follow a square-root scaling, $\mu \propto \sqrt{B}$, consistent with the relativistic Landau-level spectrum $\varepsilon_n^{(1)} \propto \sqrt{nB}$ characteristic of Dirac fermions.

For the AB-stacked bilayer in Fig. 2(b), the contour lines reveal an almost linear dependence of μ on B, indicating a scaling of the form $\mu \propto B$ while preserving the particle number. This trend reflects the bilayer Landau-level structure $\varepsilon_n^{(2)} \propto B\sqrt{n(n-1)}$, where carriers behave as massive quasiparticles with a linear field dependence at low energies.

In the trilayer case, shown in Fig. 2(c), the scaling becomes significantly steeper. The chemical potential required to maintain a fixed $\langle N\rangle$ increases rapidly with B, in agreement with the spectrum $\varepsilon_n^{(3)} \propto B^{3/2}\sqrt{n(n-1)(n-2)}$ of ABC-stacked trilayer graphene. This sharp increase arises from the high density of low-energy states and the prominent degeneracy of the zero-energy levels.

Overall, these results clarify the dependence of the particle number and chemical potential on magnetic-field strength, providing the basis for the consistent implementation of thermodynamic cycles such as the Stirling cycle, examined in the next sections.

The analysis of the energy scales and the behavior of the chemical potential in monolayer, bilayer, and trilayer graphene reveals marked differences among these systems. To enable a consistent comparison, in this work the chemical potential is adjusted as a function of temperature and magnetic field such that the particle number remains fixed:

$$N_e = \langle N(\mu(B,T),B,T)\rangle = \text{constant}. \tag{19}$$

In this manner, the particle number N_e in Eq. (19) is conserved throughout the entire thermodynamic cycle, with N_e to determine $\mu(T,B)$ within the grand–canonical framework. This choice enables a direct comparison of the distinct scaling behaviors in mono-, bi-, and trilayer graphene, thereby highlighting the physical differences that originate from their respective Landau-level structures. In this framework, the chemical potential is effectively parametrized by enforcing particle-number conservation. Applying the Maxwell relation

$$\left.\frac{d\mu}{dT}\right|_{N_e} = -\left.\frac{dS}{dN_e}\right|_{T} = 0. \tag{20}$$

It follows that the parametrized μ remains constant under temperature variations, while being nontrivially modified by the external magnetic field, as illustrated in Fig. 2.

For reference to experimental scales, we provide an order–of–magnitude estimate obtained from the magnetic length, $\ell_B = \sqrt{\hbar/(eB)}$. If N_e electrons are assumed to occupy an effective area $\pi\ell_B^2$, the corresponding sheet density can be approximated as

$$n_{2\mathrm{D}} \approx \frac{eB}{\pi\hbar}\, N_e \simeq 4.86\times 10^{10}\, N_e\, B\ \mathrm{cm}^{-2}. \tag{21}$$

For instance, at $B = 1$ T the estimated densities are $n_{2\mathrm{D}} \approx \{2.43,\ 3.89,\ 7.29\}\times 10^{11}\ \mathrm{cm}^{-2}$ for $N_e = \{5, 8, 15\}$. This correspondence is not meant to represent an exact relation but rather to serve as a practical benchmark linking the effective particle number N_e employed in the calculations with typical carrier densities reported in graphene samples.

Having established the Landau-level spectra in Eqs. 1, 3, and 5, together with the parametrized chemical potential of Eq. 19 that ensures a fixed particle number across all three systems. We now turn to the analysis of thermodynamic quantities directly relevant for the operation of quantum heat engines. In particular, we investigate how each multilayer configuration responds under thermal cycling, an aspect of central importance for the implementation of the Stirling cycle. Fig. 3 presents the internal energy of the monolayer, bilayer, and trilayer graphene as a function of temperature, for several fixed magnetic-field values and at constant particle number $N_e = 15$.

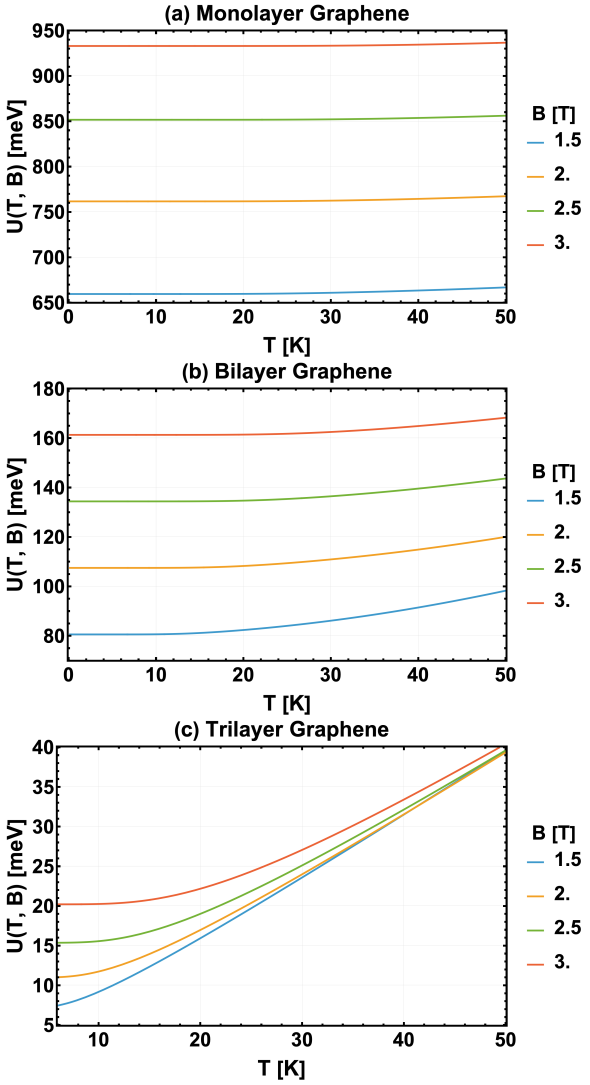

FIG. 3: Internal energy $U(T,B)$ as a function of temperature for (a) monolayer, (b) bilayer, and (c) trilayer graphene at different magnetic fields, with the particle number fixed at $N_e = 15$.

C. Thermodynamic Properties: Internal Energy and Entropy of Multilayer Graphene

Having established the Landau-level spectra in Eqs.(1, 3, 5) and the parametrized chemical potential in Eq.(19), we now turn to the analysis of thermodynamic quantities directly relevant for the operation of quantum heat engines. In particular, we examine how each multilayer configuration responds under thermal cycling, which is especially pertinent for the implementation of the Stirling cycle. The internal energy $U(T,B)$ of monolayer, bilayer, and trilayer graphene is presented in Fig. 3 as a function of temperature for several fixed magnetic-field values, at constant particle number $N_e = 15$.

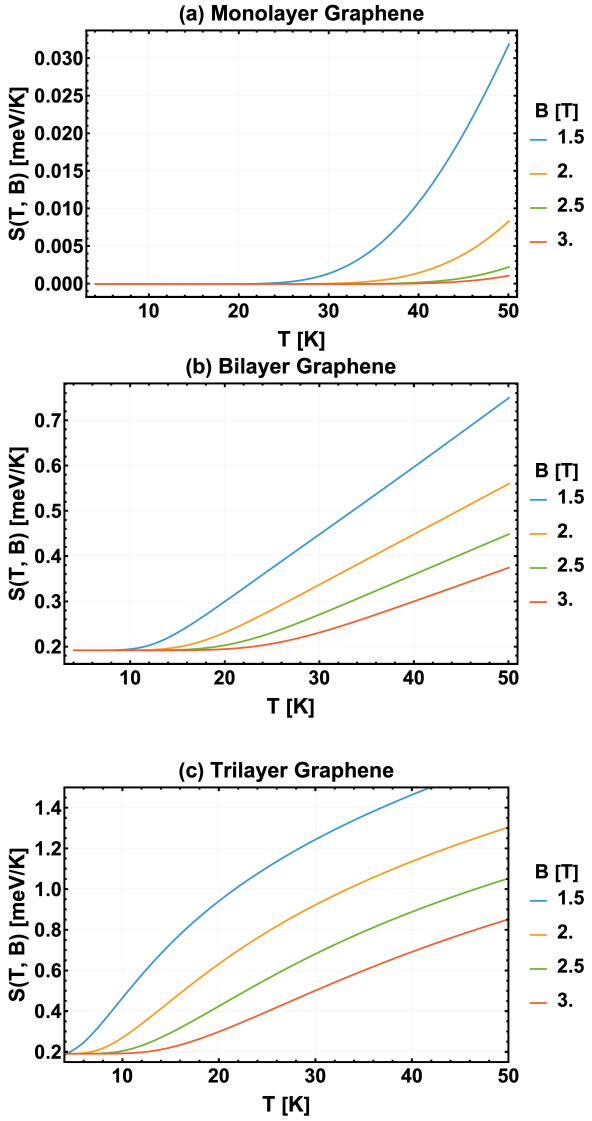

FIG. 4: Entropy $S(T, B)$ as a function of temperature for (a) monolayer, (b) bilayer, and (c) trilayer graphene at different magnetic fields, with the particle number fixed at $N_e = 15$.

In the monolayer case, shown in Fig. 3(a), the internal energy increases moderately with temperature, following a smooth and weakly nonlinear trend. This behavior reflects the relativistic nature of Dirac fermions and the square-root spacing of the Landau levels. Increasing the magnetic field enhances the Landau-level separation, which produces an upward shift in the baseline of internal energy, while the overall temperature dependence remains predominantly sublinear. For the range of fields considered, the internal energy varies between approximately 600 and 950meV. In Fig. 3(b), the bilayer system exhibits a more pronounced curvature compared to the monolayer, particularly at intermediate temperatures. At lower magnetic fields, the internal energy rises more rapidly with temperature, consistent with the parabolic band structure and the enhanced density of states near charge neutrality. Because of the smaller Landau-level separations, the states are more easily populated than in the monolayer, which increases the sensitivity of the internal energy to thermal excitations. The overall magnitude of internal energy varies between approximately 80 and 170 [meV] across the magnetic-field range considered.

In Fig. 3(c), trilayer graphene exhibits a qualitatively distinct behavior. At high temperatures, all curves display an approximately linear increase in internal energy with comparable slopes, largely independent of the magnetic field. Similar to the monolayer and bilayer cases, the separation between different B values persists throughout the entire range, with the distinction being most evident at low temperatures, indicating that magnetic-field effects remain relevant despite thermal excitations. This behavior reflects the denser and more intricate low-energy spectrum of the trilayer, which enhances the internal energy under stronger fields. Overall, the temperature dependence of the internal energy in trilayer graphene arises from a competition between two effects: the magnetic field increases the spacing between Landau levels, thereby reducing the number of thermally accessible states and suppressing the growth of internal energy; in contrast, raising the temperature promotes the occupation of higher-energy states, leading to an overall increase in internal energy. Within the explored temperature window, no crossover or inversion is observed among the curves for different magnetic fields, suggesting that neither mechanism fully dominates.

The next discussion focuses on the entropy to further characterize the thermodynamic response. Fig. 4 presents the temperature dependence of the entropy $S(T, B)$ for monolayer, bilayer, and trilayer graphene at different magnetic fields, with the particle number fixed at $N_e = 15$. While all three systems exhibit a monotonic increase of entropy with temperature, notable differences arise in magnitude, curvature, and sensitivity to the magnetic field, underscoring the distinct thermodynamic responses of each multilayer configuration. In Fig. 4(a), the entropy of monolayer graphene remains negligible at low temperatures and begins to rise appreciably only above $T \simeq 25\,\mathrm{K}$, where thermal excitations populate higher Landau levels. The increase is markedly nonlinear, particularly at lower magnetic fields. This behavior reflects the relativistic Landau-level structure where stronger magnetic fields enlarge the spacing between energy levels and thereby suppress thermal activation. Consequently, higher fields substantially reduce the entropy and produce a clear separation among the curves.

In Fig. 4(b), the bilayer case exhibits a more regular and approximately linear increase of entropy with temperature throughout the explored range. The entropy rises from about $0.2\,\mathrm{meV/K}$ to nearly $0.75\,\mathrm{meV/K}$ at the lowest field $B = 1.5\,\mathrm{T}$. The larger values compared to the monolayer reflect the denser Landau-level structure associated with the parabolic dispersion. Sensitivity to the magnetic field is also more pronounced, as stronger

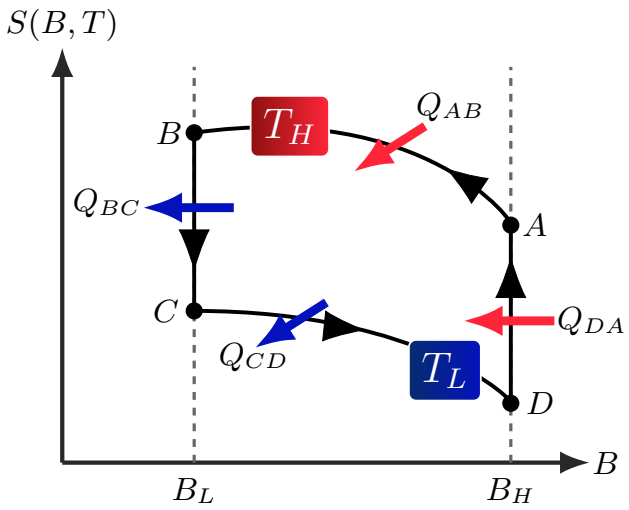

FIG. 5: Diagram of the quantum Stirling cycle in terms of entropy S and the perpendicular magnetic field B. Curves AB and CD correspond to the isotherms at $T = T_H$ and $T = T_L$, respectively. As the magnetic field increases at fixed temperature, the entropy decreases, and vice versa.

fields systematically shift the curves downward.

For the trilayer configuration shown in Fig. 4(c), the entropy starts near 0.2 meV/K and grows beyond 1.3 meV/K for $B = 1.5$ T, displaying a rapid and nonlinear increase with temperature. The entropy curves exhibit a strong dependence on the magnetic field. This behavior originates from the cubic low-energy dispersion, which generates a high density of states and reduces the spacing between adjacent energy levels, effectively producing a quasi-continuous spectrum that remains thermally active even under stronger magnetic fields.

1. *Quantum Stirling Cycle*

The quantum Stirling cycle, illustrated in Fig. 5, consists of four strokes: two isothermal and two isomagnetic processes. In this framework, the perpendicular magnetic field B acts as the external control parameter, while the working substance is assumed to remain in thermal equilibrium with the reservoirs during all stages of the cycle. The sequence of strokes is as follows:

- **(A → B)** Isothermal expansion at temperature T_H, with the magnetic field decreasing from B_H to B_L,
- **(B → C)** Isomagnetic cooling at fixed $B = B_L$, with the temperature lowered from T_H to T_L,
- **(C → D)** Isothermal compression at temperature T_L, with the magnetic field increasing from B_L to B_H,
- **(D → A)** Isomagnetic heating at fixed $B = B_H$, with the temperature raised from T_L back to T_H.

TABLE I: Sign convention for heat and work: $W > 0$ for work output, $W < 0$ for input; $Q > 0$ for heat absorbed, $Q < 0$ for heat released by the system.

Operational regime	W	Q_{out}	Q_{in}
Engine	>0	<0	>0
Refrigerator	<0	>0	<0
Accelerator	<0	<0	>0
Heater	<0	<0	<0

The heat exchanged during each stage is expressed as

$$Q_{AB} = T_H\big[S(B_L, T_H) - S(B_H, T_H)\big], \tag{22}$$
$$Q_{CD} = T_L\big[S(B_H, T_L) - S(B_L, T_L)\big], \tag{23}$$
$$Q_{BC} = U(B_L, T_L) - U(B_L, T_H), \tag{24}$$
$$Q_{DA} = U(B_H, T_H) - U(B_H, T_L), \tag{25}$$

where the labels L and H are used to distinguish the low and high values of B and T. Invoking the first law of thermodynamics, the total heat absorbed Q_{in}, the heat released Q_{out}, and the net work W per cycle can be expressed as

$$Q_{\text{in}} = Q_{AB} + Q_{DA}, \tag{26}$$
$$Q_{\text{out}} = Q_{BC} + Q_{CD}, \tag{27}$$
$$W = Q_{\text{in}} + Q_{\text{out}}. \tag{28}$$

The convention adopted here is that $Q > 0$ corresponds to heat absorbed by the system, while $W > 0$ indicates net work performed by the system. Within this framework, the efficiency of the cycle is given by

$$\eta = \frac{W}{Q_{\text{in}}} = 1 - \left|\frac{Q_{BC} + Q_{CD}}{Q_{AB} + Q_{DA}}\right|. \tag{29}$$

The physical significance of these expressions is clarified when related to the entropy behavior discussed in Sec. III C, which shows that entropy increases as the external magnetic field decreases at fixed temperature. This guarantees that the isothermal expansion stroke (A → B), performed from B_H to B_L, corresponds to a positive entropy change $\Delta S > 0$, and thus a positive heat input $Q_{AB} > 0$. In contrast, the isothermal compression stroke (C → D), carried out at lower temperature and in the reverse direction $B_L \to B_H$, yields a negative entropy change and therefore a negative heat exchange $Q_{CD} < 0$. Consequently, the different operational regimes of the engine are governed entirely by the heat contributions during the isomagnetic strokes (B → C and D → A).

Table I summarizes the adopted sign convention for heat and total work across the four operational regimes considered. In this convention, a positive total work $W > 0$ indicates that the system delivers mechanical work to the surroundings, whereas $W < 0$ corresponds to work being supplied to the system. Similarly, a positive heat $Q > 0$ denotes energy flowing into the working substance, while $Q < 0$ represents heat released to

the external reservoirs. Under these definitions, an engine operates with $W > 0$, absorbing heat from the hot reservoir ($Q_{\rm in} > 0$) and rejecting heat to the cold one ($Q_{\rm out} < 0$).

If, under the same parameters, the cycle is run in the reverse (clockwise) direction relative to Fig. 5, the device operates as a refrigerator. In this case, external work input ($W < 0$) is required to extract heat from the cold reservoir ($Q_{\rm out} > 0$) and release it to the hot reservoir ($Q_{\rm in} < 0$).

Beyond these two classical regimes, previous studies have shown that the quantum Stirling cycle may also operate in two additional regimes that arise purely from its quantum character [21, 29, 66–69]. In the *accelerator* regime, both the total work and the heat released to the cold reservoir are negative, indicating that external work input is accompanied by simultaneous heating of both reservoirs. In the *heater* regime, all heat flows are negative and $W < 0$, so that the external work is entirely dissipated as heat into both reservoirs. As will be shown in later sections, the exotic thermodynamic properties of the system, which arise from the constraint of particle number conservation, can induce these additional operational regimes.

IV. RESULTS

A. Stirling Engine Efficiency

In this section, the efficiency of the Stirling engine defined in Eq. (29) and illustrated in Fig. 5 is examined. The working substances correspond to the stacked graphene systems of Fig. 1, with the chemical potential parametrized along all strokes of the cycle to maintain a fixed particle number $N_e \in \{5, 8, 15\}$.

To quantify these effects, Fig. 6 presents the efficiency η as a function of the low magnetic field B_L for monolayer, bilayer, and trilayer graphene. For each configuration, the high magnetic field B_H and the bath temperatures T_L and T_H are kept constant as indicated in the panel captions, while the Carnot efficiency $\eta_C = 1 - T_L/T_H$ is shown as a horizontal red reference line.

In the monolayer case shown in Fig. 6(a), the conditions for the system to operate as an engine are strongly constrained for thermal reservoirs at $T_L = 50.7\,\mathrm{K}$ and $T_H = 53.85\,\mathrm{K}$, corresponding to a Carnot efficiency of $\eta_C \simeq 0.06$, with the high magnetic field fixed at $B_H = 4.0\,\mathrm{T}$. Although some curves (e.g., $N_e = 5$) can, in principle, achieve the Carnot limit with finite work, this only occurs at low carrier densities and within narrow B_L intervals. Outside these regions, the device switches to other operational regime modes and the definition of efficiency is not well defined. It is for this reason that only small intervals where the substance operates as an engine exist, while no efficiency curves are observed beyond them.

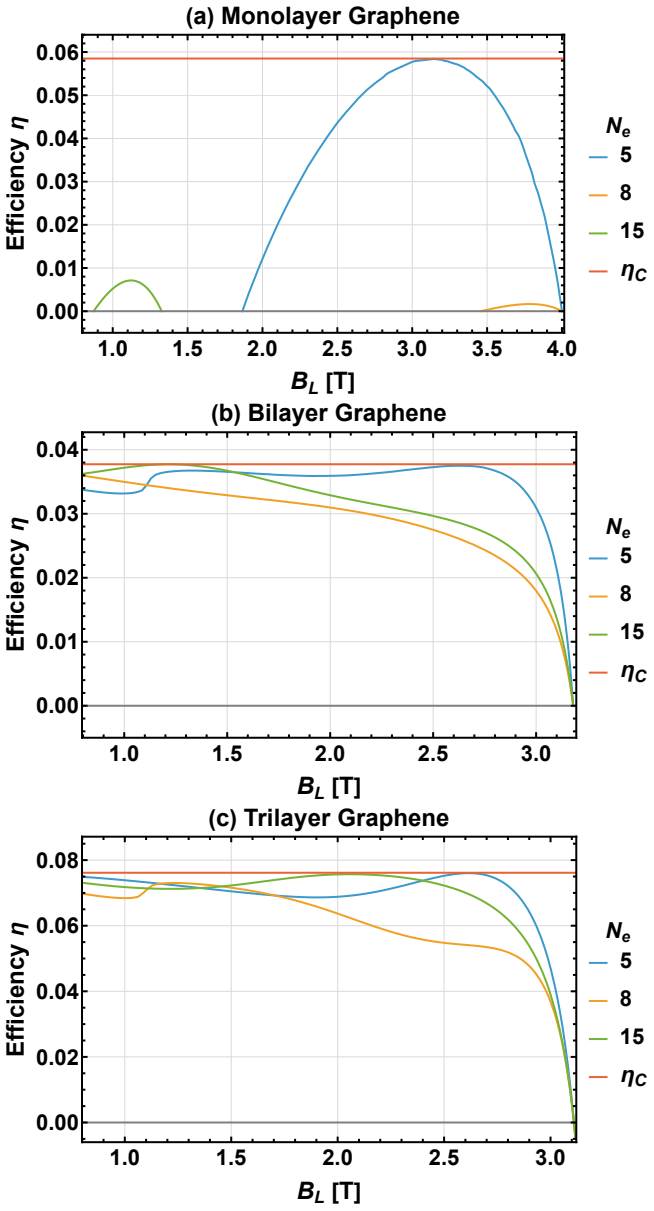

FIG. 6: Stirling engine efficiency η as a function of the low magnetic field B_L for (a) monolayer, (b) bilayer, and (c) trilayer graphene. Each panel shows results for $N_e = 5, 8, 15$ and the Carnot bound η_C. Parameters are: (a) $T_L = 50.7$ K, $T_H = 53.85$ K, $B_H = 4.0$ T, $\eta_C = 0.058$; (b) $T_L = 45.9$ K, $T_H = 47.7$ K, $B_H = 3.18$ T, $\eta_C = 0.037$; (c) $T_L = 18.2$ K, $T_H = 19.7$ K, $B_H = 3.11$ T, $\eta_C = 0.078$.

This restricted behavior can be interpreted as a consequence of the large spacing between relativistic Landau levels, which limits the thermal accessibility of higher-energy states. As a result, the heat exchanged during the isothermal strokes, while retaining the correct sign for engine operation, becomes smaller in magnitude. When the work contribution from the isomagnetic strokes surpasses that of the isothermal ones—an effect enhanced by the Landau level separation—the net work output turns neg-

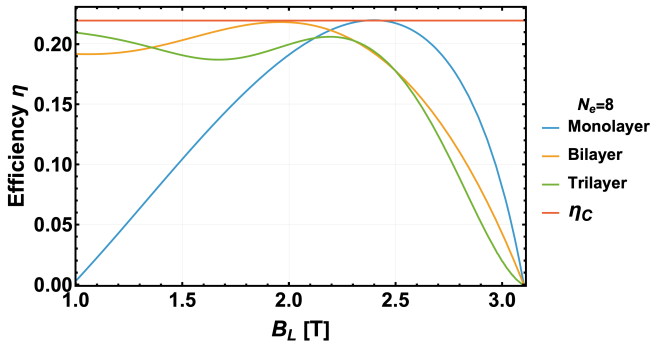

FIG. 7: Stirling engine efficiency η as a function of the low magnetic field B_L at fixed high field $B_H = 3.1$ T. Reservoir temperatures are set to $T_L = 21.3$ K, $T_H = 27.3$ K for the monolayer; $T_L = 16.7$ K, $T_H = 21.4$ K for the bilayer; and $T_L = 10.0$ K, $T_H = 12.9$ K for the trilayer. In all cases, the Carnot efficiency is $\eta_C = 0.22$.

ative and the cycle ceases to function as an engine. These exotic behaviors associated with monolayer graphene will be discussed in later sections.

For the bilayer graphene in Fig. 6(b), the system operates as an engine across the entire B_L range considered, with the high magnetic field fixed at $B_H = 3.18\,\mathrm{T}$. The thermal reservoirs are maintained at $T_L = 45.9\,\mathrm{K}$ and $T_H = 47.7\,\mathrm{K}$, corresponding to a Carnot efficiency of $\eta_C \simeq 0.04$. Under these conditions, the curves for $N_e = 5$ and $N_e = 15$ attain the Carnot bound at finite values of B_L, with the $N_e = 15$ case attaining η_C at lower B_L values than $N_e = 5$. In contrast, the $N_e = 8$ curve remains slightly below η_C over the full range, exhibiting a broad maximum just under the Carnot line at $B_L \simeq 0.8$[T]. This reflects a more balanced competition between the isothermal and isomagnetic contributions arising from the parametrization of the chemical potential. This intermediate behavior highlights how the bilayer spectrum, with its linear scaling in B, provides a broader operational window: depending on the carrier number, the cycle can either saturate the Carnot limit or remain close to it with finite work output.

For the trilayer graphene in Fig. 6(c), the high magnetic field is fixed at $B_H = 3.11\,\mathrm{T}$, while the thermal reservoirs are set at $T_L = 18.2\,\mathrm{K}$ and $T_H = 19.7\,\mathrm{K}$ with a Carnot efficiency $\eta_C \simeq 0.08$. Under these conditions, the $N_e = 15$ curve reaches the Carnot bound near $B_L \simeq 2.1\,\mathrm{T}$, whereas the $N_e = 5$ case attains η_C at $B_L \simeq 2.65\,\mathrm{T}$, closer to the upper field value $B_H = 3.18\,\mathrm{T}$. In contrast, the $N_e = 8$ curve remains consistently lower across the full range, exhibiting a broad maximum well below η_C. This behavior indicates that the enhanced zero-mode degeneracy and the steeper $B^{3/2}$ scaling of the spectrum restrict the proximity to reversible performance, with the sharpness of the response being induced by the parametrization of the chemical potential. Overall, this smoother yet less favorable trend demonstrates that, although trilayer graphene can reach Carnot efficiency for specific carrier numbers, its operational window in temperature space is narrower than in the bilayer case, and the efficiency maxima are more sensitive to the choice of N_e.

The purpose of Fig. 6 is to demonstrate, over a common range of magnetic field values, that all stacking configurations considered here are capable of reaching the Carnot efficiency. The comparison was designed such that, for each stacking, at least one of the selected particle numbers N_e attains η_C within approximately the same efficiency window. Because this requires employing similar operational temperatures across the panels, the resulting efficiencies in Fig. 6 appear relatively small. The main motivation behind this choice is to provide a direct and uniform demonstration that the Carnot bound can, in principle, be achieved in all cases, irrespective of the stacking.

In contrast, Fig. 7 focuses on the case $N_e = 8$, where all stacking configurations operate as an engine with the same fixed high magnetic field $B_H = 3.1\,\mathrm{T}$. The thermal reservoirs are chosen such that for the monolayer the temperatures are $T_L = 21.3\,\mathrm{K}$ and $T_H = 27.3\,\mathrm{K}$, for the bilayer $T_L = 16.7\,\mathrm{K}$ and $T_H = 21.4\,\mathrm{K}$, and for the trilayer $T_L = 10.0\,\mathrm{K}$ and $T_H = 12.9\,\mathrm{K}$. Despite these differences, all three cases correspond to the same Carnot efficiency, $\eta_C \simeq 0.22$.

This configuration highlights the role of carrier density in shaping the operational regime. For the trilayer, the maximum efficiency nearly reaches the Carnot limit as $B_L \to 1.0\,\mathrm{T}$ (the lowest field considered), whereas for the monolayer it occurs at higher fields, around $B_L \simeq 2.4\,\mathrm{T}$. The bilayer exhibits an intermediate response, achieving the Carnot limit near $B_L \simeq 1.9\,\mathrm{T}$. Compared to Fig. 6, which employed a uniform B_L range to demonstrate that Carnot efficiency can be reached across all stackings, the present figure emphasizes how the optimal field for reversible operation shifts significantly between systems. This contrast underscores the crucial interplay between the Landau-level spectrum and the chemical potential in determining the precise conditions under which Carnot efficiency is realized.

B. Stirling Maximum Gain

In Sec. IV A, it was shown that different graphene stackings can reach Carnot efficiency for distinct particle numbers and thermal reservoirs. However, achieving maximum efficiency does not necessarily imply maximizing the extracted work. For this reason, this section analyzes the maximum gain, defined as the product $\eta \cdot W$ (useful work), as a function of particle number and stacking configuration, while keeping the reservoirs fixed and sweeping over the same magnetic-field range. To illustrate this behavior, Fig. 8 displays contour maps of ηW as functions of the low parameters B_L and T_L, with the hot bath fixed at $T_H = 23$ K and $B_H = 4.0$ T. The rows correspond to monolayer, bilayer, and trilayer graphene,

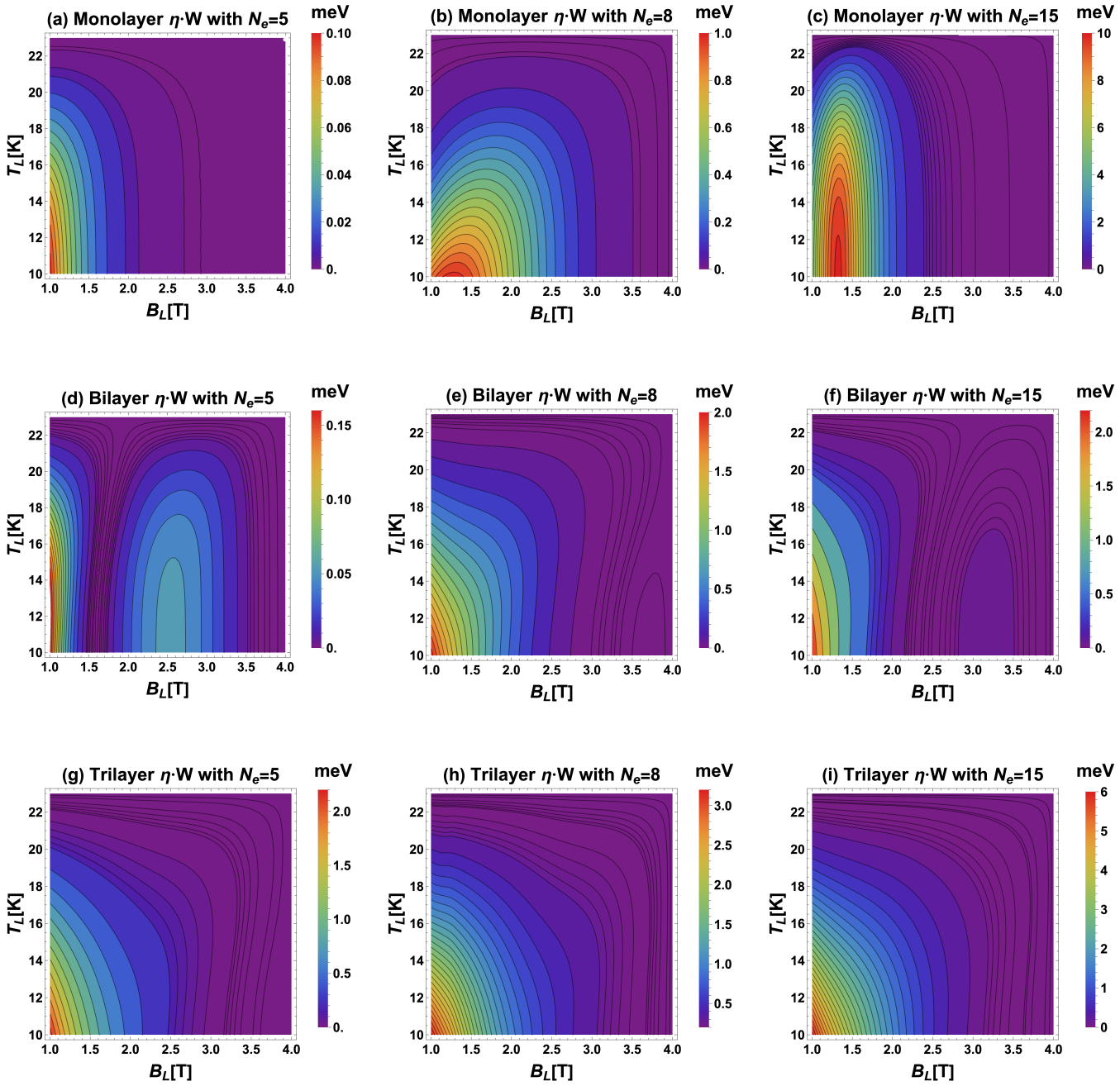

FIG. 8: Contour plots of the product $\eta \cdot W$ as a function of the low parameters B_L and T_L, with fixed high parameters $T_H = 23\,\mathrm{K}$ and $B_H = 4\,\mathrm{T}$. The panels correspond to monolayer (a)-(c), bilayer (d)-(e) and trilayer (g)-(i) graphene with (left) $N_e = 5$, (center) $N_e = 8$, and (right) $N_e = 15$.

while the columns show the cases $N_e \in \{5, 8, 15\}$. In all configurations, the best performance is concentrated at low magnetic fields ($B_L \lesssim 1.5$ T) and moderately low temperatures ($T_L \sim 10{-}15$ K), reflecting the enhancement of work and efficiency in regimes where a denser set of thermally accessible Landau levels is available.

In the monolayer case, shown in Figs. 8(a)–(c), the high-ηW region is narrow and quickly suppressed as either B_L or T_L increase. The maximum for $N_e = 5$ occurs at the lowest field and within $T_L \in 10{-}13\,\mathrm{K}$. For $N_e = 8$, the favorable region expands slightly in field range ($B_L \in 1.0{-}1.5\,\mathrm{T}$) but narrows in temperature ($T_L \in 10{-}11\,\mathrm{K}$). At $N_e = 15$, the contour shrinks again in field range relative to $N_e = 8$, though it widens in temperature ($T_L \in 10{-}14\,\mathrm{K}$). The maximum values also increase markedly with particle number, from about

0.1 meV at $N_e = 5$ to 1.0 meV at $N_e = 8$, and nearly 10 meV at $N_e = 15$.

For bilayer graphene, illustrated in Figs. 8(d)–(f), the optimum broadens into a smoother, rounded peak, indicating a wider operational window consistent with the enhanced density of states. For $N_e = 5$, the maximum again appears near the lowest field but over a broader temperature range ($T_L \simeq 10$–15 K), together with a secondary plateau around $B_L \simeq 2.5$ T. For $N_e = 8$, the maximum shifts back to very low fields and a narrow window of $T_L \simeq 10$–11 K. At $N_e = 15$, the contours resemble the previous case but display a low-ηW pocket at $B_L \simeq 2.8$–3.4 T. The scaling with particle number differs from the monolayer: the maxima are 0.15 meV for $N_e = 5$, 2.0 meV for $N_e = 8$, but remain at 2.0 meV for $N_e = 15$, showing saturation rather than continued growth.

The trilayer configuration, depicted in Figs. 8(g)–(i), sustains sizable values of ηW over a comparable B_L range and extends to slightly higher T_L. At $N_e = 5$, the maximum is located near the lowest field and around $T_L \simeq 10$ K, reaching 2.0 meV. For $N_e = 8$, the contours broaden both in field and temperature, with the maximum increasing to 3.0 meV. At $N_e = 15$, the pattern closely resembles the $N_e = 8$ case but with a higher maximum of about 6.0 meV, still significantly smaller than the monolayer for the same particle number. This reduction is a direct consequence of the smaller Landau-level spacing and lower energy scale in the trilayer system.

C. Stirling Operational Regimes

In the previous sections, the working substances were shown to operate as engines with high efficiency and significant work extraction. Nevertheless, these systems may also display exotic behaviors, leading to the emergence of different operational regimes. To illustrate this point, Fig. 9 presents the operational map of the Stirling cycle for monolayer graphene at fixed $B_H = 3.0$ T, $T_L = 46$ K, and $N_e = 5$. Within the explored window of low magnetic field B_L and hot reservoir temperature T_H, no engine region is observed. Instead, the diagram reveals a small refrigerator domain at $B_L \simeq 0.7$–1.8 T and $T_H \simeq 46$–49.5 K, two accelerator wedges near the lowest and highest values of B_L, and a broad heater region covering most of the parameter space.

The absence of engine operation indicates that, under these conditions, heat exchange in the isomagnetic strokes dominates over the isothermal contributions. This outcome reflects both the wide spacing of relativistic Landau levels and the parametrization of the chemical potential imposed to maintain $N_e = 5$ throughout the cycle. Consequently, the system exhibits $W < 0$ across the entire diagram, with the specific regime determined by the balance of heat flows: refrigerator, accelerator, or heater. These results align with the performance maps in Fig. 8, where the monolayer shows weak ηW values and a

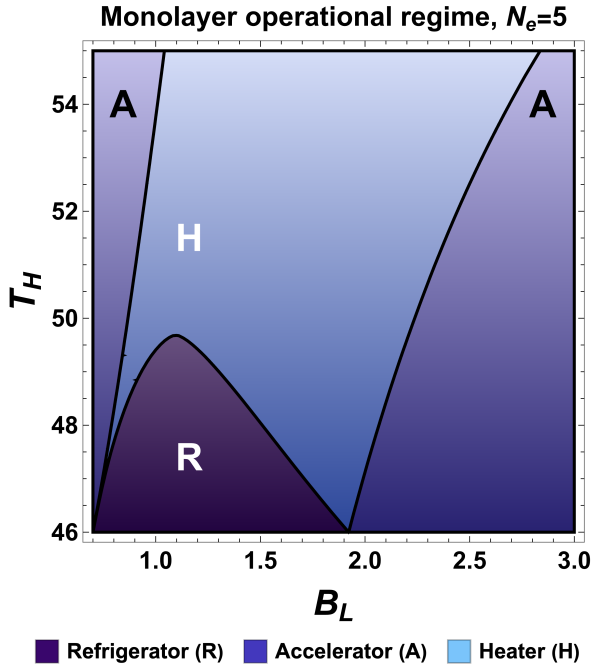

FIG. 9: Operational regimes of the Stirling cycle for monolayer graphene with $N_e = 5$, as functions of the low magnetic field B_L and hot reservoir temperature T_H, at fixed $B_H = 3.0$ T and $T_L = 46$ K.

rapidly vanishing optimum, as well as with the efficiency curves in Fig. 6, which display only small, low-efficiency engine regions and predominantly non-engine behavior. Engine windows may emerge under different parameter choices, but are absent in the present configuration.

It should be emphasized that realizing different operational regimes in bilayer and trilayer graphene would require substantially lower temperatures and much higher magnetic fields than those explored in this study, owing to their smaller characteristic energy scales. Accordingly, the present analysis focuses on regimes accessible at comparatively higher temperatures, which are not only more relevant for the purposes of this work but also more feasible from an experimental perspective.

V. CONCLUSIONS AND DISCUSSION

In this study, quantum Stirling cycles in monolayer, AB-stacked bilayer, and ABC-stacked trilayer graphene under perpendicular magnetic fields were investigated within a grand-canonical, fully fermionic framework based on the exact Landau spectra. An order-of-magnitude comparison between the particle number N_e, the chemical potential employed in the simulations, and sheet carrier densities defined by the magnetic length indicates that the most favorable regimes are experimentally accessible.

Thermodynamic quantities, including internal energy and entropy, were consistently evaluated using

Fermi–Dirac statistics, with the chemical potential $\mu(T, B)$ parametrized to conserve particle number along both isothermal and isomagnetic branches. In this framework, the perpendicular magnetic field acted as the external control parameter driving the cycle.

Across the explored parameter space and for multiple fixed particle numbers, the monolayer and the stacked configurations demonstrated the capacity to reach Carnot efficiency under suitable magnetic conditions. Among them, the AB bilayer exhibited the broadest operational window and reached the Carnot bound while sustaining finite work output, whereas the monolayer showed more constrained operation and the trilayer presented smoother efficiency trends with sizable values of the combined performance metric ηW over a comparable B_L range.

Overall, the monolayer Stirling cycle, due to its larger Landau-level spacing and higher characteristic energy scale, delivered greater useful work at higher efficiency compared with the bilayer and trilayer cases. Its capability to operate across all thermodynamic regimes as an engine, refrigerator, heater, and accelerator highlights its versatility. This feature suggests possible applications, such as employing the monolayer cycle to cool other working substances including quantum batteries or supercondensates, while simultaneously acting as a heater at elevated temperatures.

Acknowledgments

B.C, F.J.P., M.H.G, N.C, and P.V. acknowledge financial support from ANID Fondecyt grant no. 1240582. B.C, F.J.P., M.H.G, and P.V. acknowledge financial support from ANID Fondecyt grant no. 1250173. B.C acknowledge PUCV and Programa de Incentivo a la Iniciación Científica (PIIC) no. 004 from "Dirección de Postgrado" of UTFSM. B.C. acknowledges the support of ANID Becas/Doctorado Nacional 21250015. C.L. thanks the support by the Brazilian agencies CNPq and FAPERJ.

[1] S. Vinjanampathy and J. Anders, Quantum thermodynamics, Contemporary Physics **57**, 545 (2016).
[2] R. Kosloff, Quantum thermodynamics: A dynamical viewpoint, Entropy **15**, 2100 (2013).
[3] S. Deffner and S. Campbell, *Quantum Thermodynamics: An Introduction to the Thermodynamics of Quantum Information* (Morgan & Claypool Publishers, 2019).
[4] J. Millen and A. Xuereb, Perspective on quantum thermodynamics, New J. Phys. **18**, 011002 (2016).
[5] F. Binder, S. Vinjanampathy, K. Modi, and J. Goold, Quantum thermodynamics of general quantum processes, Phys. Rev. E **91**, 032119 (2015).
[6] F. Binder, L. A. Correa, C. Gogolin, J. Anders, and G. Adesso, Thermodynamics in the quantum regime, in *Fundamental Theories of Physics*, Vol. 195 (Springer, 2018).
[7] N. M. Myers, O. Abah, and S. Deffner, Quantum thermodynamic devices: From theoretical proposals to experimental reality, AVS Quantum Science **4**, 027101 (2022).
[8] G. L. Zanin, T. Haffner, M. A. A. Talarico, E. I. Duzzioni, P. H. Souto Ribeiro, G. T. Landi, and L. C. Celeri, Experimental quantum thermodynamics with linear optics, Braz. J. Phys. **49**, 783 (2019).
[9] C. H. S. Vieira, J. L. D. de Oliveira, J. F. G. Santos, P. R. Dieguez, and R. M. Serra, Exploring quantum thermodynamics with NMR, J. Magn. Reson. Open **16-17**, 100105 (2023).
[10] G. De Chiara, G. Landi, A. Hewgill, B. Reid, A. Ferraro, A. J. Roncaglia, and M. Antezza, Reconciliation of quantum local master equations with thermodynamics, New J. Phys. **20**, 113024 (2018).
[11] B. Castorene, F. J. Peña, A. Norambuena, S. E. Ulloa, C. Araya, and P. Vargas, Entropy, entanglement, and susceptibility of three qubits near quantum criticality, Phys. Rev. E **111**, 034118 (2025).
[12] G. Ford and R. O'Connell, Entropy of a quantum oscillator coupled to a heat bath and implications for quantum thermodynamics, PHYSICA E-LOW-DIMENSIONAL SYSTEMS & NANOSTRUCTURES **29**, 82 (2005), international Conference on Frontiers of Quantum and Mesoscopic Thermodynamics (FQMT04), Prague, CZECH REPUBLIC, JUL 26-29, 2004.
[13] P. Liuzzo-Scorpo, L. A. Correa, R. Schmidt, and G. Adesso, Thermodynamics of quantum feedback cooling, ENTROPY **18**, 48 (2016).
[14] C. Syros, Quantum thermodynamics -: H-theorem and the second law, LETTERS IN MATHEMATICAL PHYSICS **50**, 29 (1999).
[15] F. Brandao, M. Horodecki, N. Ng, J. Oppenheim, and S. Wehner, The second laws of quantum thermodynamics, PROCEEDINGS OF THE NATIONAL ACADEMY OF SCIENCES OF THE UNITED STATES OF AMERICA **112**, 3275 (2015).
[16] H. Saygin and A. Sisman, Quantum degeneracy effect on the work output from a Stirling cycle, J. Appl. Phys. **90**, 3086 (2001).
[17] A. Sisman and H. Saygin, Efficiency analysis of a Stirling power cycle under quantum degeneracy conditions, Phys. Scr. **63**, 263 (2001).
[18] C. Cruz, H.-R. Rastegar-Sedehi, M. F. Anka, T. R. de Oliveira, and M. Reis, Quantum Stirling engine based on dinuclear metal complexes, Quantum Science and Technology **8**, 035010 (2023).
[19] S. H. Raja, S. Maniscalco, G.-S. Paraoanu, J. P. Pekola, and N. Lo Gullo, Finite-time quantum Stirling heat engine, New J. Phys. **23**, 033034 (2021).
[20] S. Cakmak and H. R. R. Sedehi, Construction of a quantum Stirling engine cycle tuned by dynamic-angle spinning, Phys. Scr. **98**, 105921 (2023).
[21] B. Castorene, F. J. Pena, A. Norambuena, S. E. Ulloa, C. Araya, and P. Vargas, Effects of magnetic anisotropy on three-qubit antiferromagnetic thermal ma-

chines, Phys. Rev. E **110**, 044135 (2024).
[22] Y. Yin, L. Chen, and F. Wu, Performance of quantum stirling heat engine with numerous copies of extreme relativistic particles confined in 1d potential well, PHYSICA A-STATISTICAL MECHANICS AND ITS APPLICATIONS **503**, 58 (2018).
[23] N. Papadatos, Quantum stirling heat engine with squeezed thermal reservoir, CHINESE PHYSICS B **32**, 100702 (2023).
[24] F. Wu, L. Chen, F. Sun, C. Wu, and Y. Zhu, Performance and optimization criteria for forward and reverse quantum stirling cycles, ENERGY CONVERSION AND MANAGEMENT **39**, 733 (1998).
[25] H.-R. Rastegar-Sedehi, N. Papadatos, and C. Cruz, Universal quantum stirling-like engine under squeezed thermal baths, EUROPEAN PHYSICAL JOURNAL PLUS **140**, 199 (2025).
[26] Z. Huang, F. Wu, L. Chen, C. Wu, and F. Guo, Performance optimization for an irreversible quantum stirling cooler, JOURNAL OF THERMAL SCIENCE **11**, 193 (2002).
[27] S. Xia, M. Lv, Y. Pan, J. Chen, and S. Su, Performance improvement of a fractional quantum stirling heat engine, JOURNAL OF APPLIED PHYSICS **135**, 034302 (2024).
[28] P. D. Li, G. Y. Ding, J. Q. Zhang, Q. Yuan, S. Q. Dai, T. H. Cui, F. Zhou, L. Chen, Q. Zhong, H. Jing, S. K. Ozdemir, and M. Feng, Experimental demonstration of single-spin Stirling engine cycles with enhanced efficiency, Phys. Rev. A **111**, L010203 (2025).
[29] C. Araya, F. J. Pena, A. Norambuena, B. Castorene, and P. Vargas, Magnetic stirling cycle for qubits with anisotropy near the quantum critical point, TECHNOLOGIES **11**, 169 (2023).
[30] S. Chatterjee, A. Koner, S. Chatterjee, and C. Kumar, Temperature-dependent maximization of work and efficiency in a degeneracy-assisted quantum stirling heat engine, Phys. Rev. E **103**, 062109 (2021).
[31] H. W. Zhang, X. L. Huang, and S. L. Wu, Quantum heat engine with identical particles and level degeneracy, INTERNATIONAL JOURNAL OF MODERN PHYSICS B **38**, 10.1142/S0217979224501091 (2024).
[32] S. Koyanagi and Y. Tanimura, Thermodynamic quantum fokker-planck equations and their application to thermostatic stirling engine, JOURNAL OF CHEMICAL PHYSICS **161**, 112501 (2024).
[33] F. J. Peña, O. Negrete, G. Alvarado-Barrios, D. Zambrano, A. González, A. S. Nunez, P. A. Orellana, and P. Vargas, Magnetic Otto engine for an electron in a quantum dot: Classical and quantum approach, Entropy **21**, 512 (2019).
[34] S. Deffner, Efficiency of harmonic quantum Otto engines at maximal power, Entropy **20**, 875 (2018).
[35] A. H. Castro Neto, F. Guinea, N. M. Peres, K. S. Novoselov, and A. K. Geim, The electronic properties of graphene, Rev. Mod. Phys. **81**, 109 (2009).
[36] M. O. Goerbig, Electronic properties of graphene in a strong magnetic field, Rev. Mod. Phys. **83**, 1193 (2011).
[37] E. McCann and V. I. Fal'ko, Landau-level degeneracy and quantum Hall effect in a graphite bilayer, Phys. Rev. Lett. **96**, 086805 (2006).
[38] H. Min and A. H. MacDonald, Electronic Structure of Multilayer Graphene, Progress of Theoretical Physics Supplement **176**, 227 (2008).
[39] S. Yuan, R. Roldán, and M. I. Katsnelson, Landau level spectrum of ABA- and ABC-stacked trilayer graphene, Phys. Rev. B **84**, 125455 (2011).
[40] A. Mani, S. Pal, and C. Benjamin, Designing a highly efficient graphene quantum spin heat engine, Scientific Reports **9**, 6018 (2019).
[41] A. Singh and C. Benjamin, Magic angle twisted bilayer graphene as a highly efficient quantum Otto engine, Phys. Rev. B **104**, 125445 (2021).
[42] N. M. Myers, F. J. Peña, N. Cortés, and P. Vargas, Multilayer graphene as an endoreversible Otto engine, Nanomaterials **13**, 1548 (2023).
[43] M. Koshino and T. Ando, Magneto-optical properties of multilayer graphene, Phys. Rev. B **77**, 115313 (2008).
[44] M. Nakamura and L. Hirasawa, Electric transport and magnetic properties in multilayer graphene, Phys. Rev. B **77**, 045429 (2008).
[45] V. Ghai, S. Pashazadeh, H. Ruan, and R. Kadar, Orientation of graphene nanosheets in magnetic fields, PROGRESS IN MATERIALS SCIENCE **143**, 101251 (2024).
[46] F. P. Riffo, S. Vizcaya, E. Menendez-Proupin, J. M. Florez, L. Chico, and E. S. Morell, Behavior of localized states in double twisted ABC trilayer graphene, Carbon **222**, 118952 (2024).
[47] P. Rickhaus, M. Weiss, L. Marot, and C. Schoenenberger, Quantum Hall effect in graphene with superconducting electrodes, Nano Lett. **12**, 1942 (2012).
[48] D. Jahani, O. Akhavan, and A. Ghatar, Optical quantum Hall goos-hanchen effect in graphene, Phys. Lett. A **465**, 128700 (2023).
[49] D. Valenzuela, S. Hernandez-Ortiz, M. Loewe, and A. Raya, Graphene transparency in weak magnetic fields, JOURNAL OF PHYSICS A-MATHEMATICAL AND THEORETICAL **48**, 065402 (2015).
[50] F. Peng, Magnetic moment of phonons in graphene induced by a magnetic field, PHYSICA B-CONDENSED MATTER **406**, 2107 (2011).
[51] W. Bao, L. Jing, J. Velasco Jr, Y. Lee, G. Liu, D. Tran, B. Standley, M. Aykol, S. Cronin, D. Smirnov, *et al.*, Stacking-dependent band gap and quantum transport in trilayer graphene, Nat. Phys. **7**, 948 (2011).
[52] M. Josefsson, A. Svilans, A. M. Burke, E. A. Hoffmann, S. Fahlvik, C. Thelander, M. Leijnse, and H. Linke, A quantum-dot heat engine operating close to the thermodynamic efficiency limits, Nature Nanotechnology **13**, 920 (2018).
[53] M. Josefsson and M. Leijnse, Double quantum-dot engine fueled by entanglement between electron spins, Phys. Rev. B **101**, 081408 (2020).
[54] P. A. Erdman, F. Mazza, R. Bosisio, G. Benenti, R. Fazio, and F. Taddei, Thermoelectric properties of an interacting quantum dot based heat engine, Phys. Rev. B **95**, 245432 (2017).
[55] M. Josefsson, A. Svilans, H. Linke, and M. Leijnse, Optimal power and efficiency of single quantum dot heat engines: Theory and experiment, Phys. Rev. B **99**, 235432 (2019).
[56] O. Arroyo-Gascon, R. Fernandez-Perea, E. S. Morell, C. Cabrillo, and L. Chico, Universality of moiré physics in collapsed chiral carbon nanotubes, Carbon **205**, 394 (2023).
[57] N. G. Kalugin, L. Jing, E. Suarez Morell, G. C. Dyer, L. Wickey, M. Ovezmyradov, A. D. Grine, M. C. Wanke,

E. A. Shaner, C. N. Lau, L. E. F. Foa Torres, M. V. Fistul, and K. B. Efetov, Photoelectric polarization-sensitive broadband photoresponse from interface junction states in graphene, 2D MATERIALS **4**, 015002 (2017).

[58] M. Pelc, E. Suarez Morell, L. Brey, and L. Chico, Electronic conductance of twisted bilayer nanoribbon flakes, JOURNAL OF PHYSICAL CHEMISTRY C **119**, 10076 (2015).

[59] E. Suarez Morell and L. E. F. Foa Torres, Radiation effects on the electronic properties of bilayer graphene, Phys. Rev. B **86**, 125449 (2012).

[60] M. Esposito, R. Kawai, K. Lindenberg, and C. Van den Broeck, Quantum-dot Carnot engine at maximum power, Phys. Rev. E **81**, 041106 (2010).

[61] B. De and B. Muralidharan, Thermoelectric study of dissipative quantum-dot heat engines, Phys. Rev. B **94**, 165416 (2016).

[62] J. Du, W. Shen, X. Zhang, S. Su, and J. Chen, Quantum-dot heat engines with irreversible heat transfer, Phys. Rev. Research **2**, 013259 (2020).

[63] F. J. Peña, D. Zambrano, O. Negrete, G. De Chiara, P. A. Orellana, and P. Vargas, Quasistatic and quantum-adiabatic Otto engine for a two-dimensional material: The case of a graphene quantum dot, Phys. Rev. E **101**, 012116 (2020).

[64] M. Koshino and T. Ando, Quantum Hall effect in graphene, INTERNATIONAL JOURNAL OF MODERN PHYSICS B **21**, 1140 (2007).

[65] A. Jellal, Integer quantum Hall effect in graphene, Phys. Lett. A **380**, 1514 (2016).

[66] H.-R. Rastegar-Sedehi and C. Cruz, Exploring entanglement effects in a quantum Stirling heat engine, Phys. Scr. **99**, 125936 (2024).

[67] B. Castorene, V. G. de Paula, F. J. Pena, C. Cruz, M. Reis, and P. Vargas, Quantum level-crossing induced by anisotropy in spin-1 heisenberg dimers: Applications to quantum stirling engines, ADVANCED QUANTUM TECHNOLOGIES 10.1002/qute.202500204 (2025).

[68] H. R. Rastegar-Sedehi and C. Cruz, Entangled quantum stirling heat engine based on two particles heisenberg model with dzyaloshinskii-moriya interaction, FRONTIERS IN PHYSICS **13**, 1512998 (2025).

[69] G. Behrendt and S. Deffner, Endoreversible stirling cycles: Plasma engines at maximal power, ENTROPY **27**, 807 (2025).